Power Electronic Systems
Laboratory

Proceedings of the International Conference on Renewable Energy Research and Applications (ICRERA 2012), Nagasaki, Japan, November 11-14, 2012

Comparative Evaluation of Control Methods for Inductive Power Transfer

R. Bosshard,
U. Badstübner,
J. W. Kolar,
I. Stevanovic

Eidgenössische Technische Hochschule Zürich
Swiss Federal Institute of Technology Zurich

Comparative Evaluation of Control Methods for Inductive Power Transfer

R. Bosshard*, U. Badstübner*, J. W. Kolar*, and I. Stevanović†
*Power Electronic Systems Laboratory, ETH Zürich, Switzerland, Email: bosshard@lem.ee.ethz.ch
†ABB Switzerland Ltd., Corporate Research, 5405 Baden-Dättwil, Switzerland

***Abstract*—Inductive Power Transfer (IPT) has recently been proposed for application with Electric or Hybrid Electric Vehicles (EV/HEV), where a highly efficient system operation is demanded for the high-power transfer. Due to the high requirements on the regulation of the output power and the output voltage, and due to the large variations of the magnetic coupling, the control of these systems is a challenging task. In this paper, the frequency characteristics of a series-parallel compensated IPT system are discussed. Different control methods found in the literature are analyzed and a comparative evaluation of the current and voltage stress in the transmission coils, the resonant capacitors, and the semiconductors in the primary-side inverter is presented. It is shown that the dual control method offers a number of advantages in the controllability and potentially lower losses compared to the frequency control which is commonly used.**

I. Introduction

The first modern Inductive Power Transfer (IPT) systems have been developed as early as 1960 [1], [2] for applications mainly in biomedical and radio-frequency identification systems [3]–[6], where they were used as power supply for implanted devices and for remote sensors. IPT is being used as a battery charging technology for consumer electronic devices [7] and, more recently, it was proposed for charging the batteries of Electric or Hybrid Electric Vehicles (EV/HEV) [8]–[10]. Besides the limited vehicle range, the inconvenient and possibly hazardous cable-connected recharging of the traction battery are a major concern for many potential EV/HEV users. IPT offers the possibility to overcome these limitations and promote the use of electric instead of fossil-fuelled vehicles.

The design as well as the efficient operation of these systems are a major challenge due to the wide-range Operating Area (OA): in practical IPT systems, the magnetic coupling of the transmission coils varies drastically if the coils are not perfectly aligned. Moreover, the terminal voltage of the batteries that are commonly used in EV/HEV (e.g. NiMH or Li-ion) may vary up to 50% in dependency of the state-of-charge due to internal chemical effects [11]. The charging controller must additionally adapt the output power according to a charging profile adapted to the battery in order to prevent damaging the cells. As illustrated in Fig. 1(a), these variations lead to a very large OA regarding output voltage U_{out}, output power P_{out} and magnetic coupling k, and make the optimal design of the IPT system a challenging task.

A number of design and control guidelines have been presented in recent publications [10], [12]–[14]. In this paper possible control schemes found in literature are evaluated and compared according to the following performance criteria: efficiency, component stress and controllability of the power electronic system. A fundamental frequency analysis of the IPT system shown in Fig. 1(c) is presented in Section II and reviewed in Section III. Three possible control methods, a) phase shift control at a fixed switching frequency, b) frequency control, and c) dual control, are discussed in Section IV and their performance is evaluated and compared in Section V.

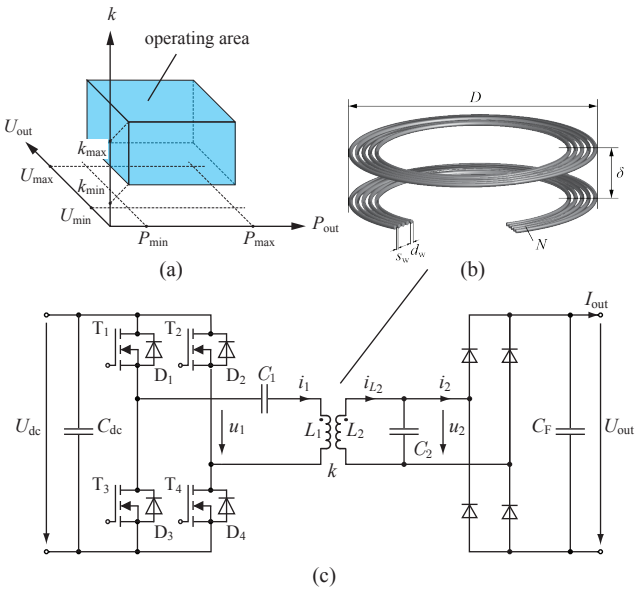

Fig. 1. Operating area of the IPT system, defined by minimum and maximum values of the output power P_{out}, output voltage U_{out}, and magnetic coupling k (a); considered circular spiral coil design (b), and circuit topology with a series-parallel compensation of the coils (c).

II. IPT System

A set of circular spiral coils as shown in Fig. 1(b), is considered as transmission coils of the analyzed IPT system. According to typical specifications of a traction battery, the system is designed for an output voltage of 400-600 V and an output power of up to 5 kW (cf. Table I). A full-bridge inverter that is fed from a 400 V dc-link can be used as supply at the primary side. At this power level and operating frequency, MOSFETs are the most suitable switching devices. A diode rectifier with a capacitive filter is used to produce the required dc-voltage at the output. The choice of the compensation topology and the required component values of the resonant elements as given in Table I are derived in the following.

A fundamental requirement to achieve the maximum possible efficiency is the matching of the receiver-coil inductance L_2 to the equivalent load resistance R_{L} according to the condition

$$L_2 = \frac{R_{\text{L}}}{\omega_0 \gamma_{\text{opt}}}, \tag{1}$$

where ω_0 is the desired resonant frequency and $\gamma_{\text{opt}} \approx 3.63$ is the optimal matching factor for the considered coil set at the maximum coupling $k_{\text{max}} = 0.3$ and an assumed inductor quality factor of $Q = 300$ and quality ratio $q = 1$ (cf. [7], [15]).

To reduce the required inductance value and, thus, the required inductor size, a parallel-compensation of the receiver is preferable over

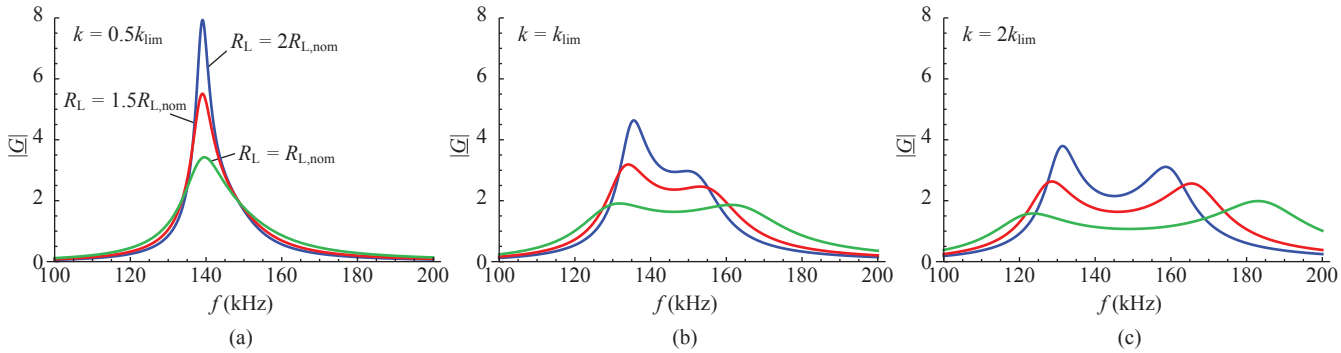

Fig. 2. Magnitude of the voltage transfer function $\underline{G}$ shown for different values of the equivalent load resistance R_L and for magnetic coupling values (a) $k = 0.5k_\mathrm{lim}$, (b) $k = k_\mathrm{lim}$ and (c) $k = 2k_\mathrm{lim}$, where $R_\mathrm{L,nom} = 58.4\,\Omega$ is the value at $U_\mathrm{out,max}/P_\mathrm{out,max}$ and k_lim is obtained by (8). A single peak of the characteristics occurs if k is below k_lim, above this limit two peaks can be observed.

TABLE I
SYSTEM SPECIFICATIONS

Symbol	Quantity	Value
U_dc	dc-link voltage	400 V
U_out	output voltage range	400 - 600 V
P_out	output power range	1 - 5 kW
f_0	resonant frequency	140 kHz
k	magnetic coupling range	0.1 - 0.3
L_1	primary inductance	90.2 µH
C_1	primary capacitance	14.4 nF
L_2	secondary inductance	18.3 µH
C_2	secondary capacitance	64.9 nF

a series-compensation at the specified output power and voltage levels [3]. To achieve a high partial load efficiency, a series-compensation at the primary side is chosen, which leads to the circuit topology shown in Fig. 1(c).

The optimal value of the parallel-compensation capacitor C_2 in this case is [4]

$$C_2 = \frac{1}{2\omega_0^2 L_2}\left(1+\sqrt{1-4\left(\frac{\omega_0 L_2}{R_\mathrm{L}}\right)^2}\right). \tag{2}$$

The inductance ratio $n = \sqrt{L_1/L_2}$ can be used to adjust the desired output voltage to the dc-link voltage. The lower limit

$$n \geq \frac{1}{k_\mathrm{max}}\frac{U_\mathrm{dc}}{U_\mathrm{out,max}}, \tag{3}$$

where $k_\mathrm{max} = 0.3$ and $U_\mathrm{out,max} = 600\,\mathrm{V}$ according to Table I, was used for designing L_1. The series-compensation capacitor on the primary is determined as [15]

$$C_1 = \frac{1}{\omega_0^2 L_1} \tag{4}$$

in order to compensate the reactance of the primary inductance.

III. FUNDAMENTAL FREQUENCY ANALYSIS

According to [16], a resistive load with a diode rectifier and a capacitive output filter operating at a constant output power P_out and output voltage U_out can be modelled by the equivalent resistance R_L with

$$R_\mathrm{L} = \frac{8}{\pi^2}\frac{U_\mathrm{out}^2}{P_\mathrm{out}}. \tag{5}$$

Even though this model neglects the effect of the output capacitor on the phase angle between the fundamentals of the rectifier input voltage and current [17], it is sufficient for a first, simplified analysis.

Using the fundamental frequency model, the input impedance of the resonant tank

$$\underline{Z}_\mathrm{in} = \frac{\hat{\underline{U}}_{1(1)}}{\hat{\underline{I}}_{1(1)}} = R_\mathrm{in} + \mathrm{j}X_\mathrm{in} \tag{6}$$

can be calculated from the equivalent circuit. Additionally, the transfer function

$$\underline{G} = \frac{\hat{\underline{U}}_{2(1)}}{\hat{\underline{U}}_{1(1)}} \tag{7}$$

can be derived from the ratio of the fundamental of the rectifier-side voltage $\hat{\underline{u}}_{2(1)}$ and the fundamental of the inverter output voltage $\hat{\underline{u}}_{1(1)}$.

Fig. 2 shows the magnitude of $\underline{G}$ in dependency of the operating frequency for different values of the magnetic coupling and the equivalent load resistance. While operating below

$$k_\mathrm{lim} \approx \frac{\omega_0 L_2}{R_\mathrm{L}}, \tag{8}$$

the curves show only a single peak, cf. Fig. 2(a), whereas if $k \geq k_\mathrm{lim}$ as shown in Fig. 2(b)-(c), a second peak appears. This pole-splitting phenomenon was first analyzed in [18]. It was shown that if the magnetic coupling exceeds a certain limit k_lim, the reactive part of the input impedance X_in exhibits three zero crossings instead of just one. In more recent literature, this is often termed the bi-furcation phenomenon, e.g. [13]. For a series compensated receiver circuit, the limit can be calculated analytically by $k_\mathrm{lim} = R_\mathrm{L}/(\omega_0 L_2)$ [18]. For a parallel compensated receiver circuit an analytical calculation of the limit value is difficult, however, (8) has proven to be a good approximation (cf. Fig. 3).

Depending on the respective output voltage and the output power limits as given in Table I, the limit k_lim is in the range $k_\mathrm{lim} \in [0.05...0.62]$. Fig. 3(a) shows the magnitude of the voltage transfer function as a function of the operating frequency for four magnetic coupling values (constant R_L). In Fig. 3(b)-(c) the magnitude $|\underline{Z}_\mathrm{in}|$ and the phase of the input impedance φ are shown for the same values. It can be seen that for $k \geq k_\mathrm{lim}$, the phase exhibits three zero crossings, whereas at $k < k_\mathrm{lim}$ only one zero crossing exists.

According to (8), this phenomenon can be reduced by choosing a higher resonant frequency or a receiver coil with a high inductance.

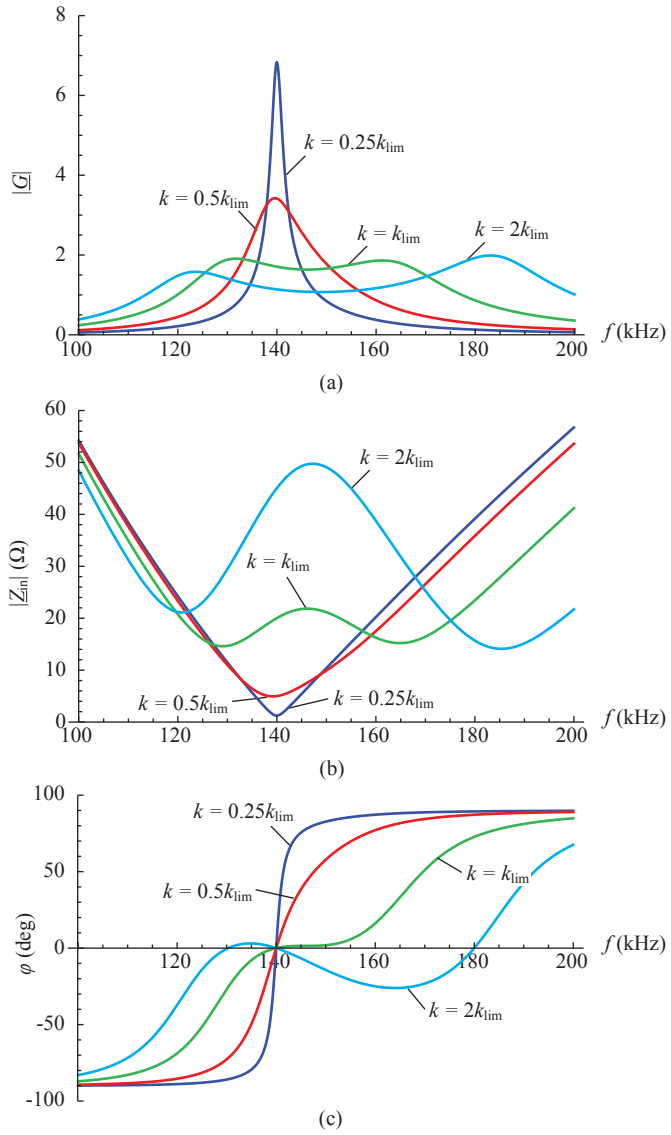

Fig. 3. The magnitude of the voltage transfer function $|\underline{G}|$ (a), the magnitude $|\underline{Z}_{\text{in}}|$ (b) and the phase $\varphi = \arg(\underline{Z}_{\text{in}})$ (c) of the input impedance at the equivalent load resistance $R_{\text{L,nom}} = 58.4\,\Omega$. For values $k < k_{\text{lim}}$ only a single peak appears in $\underline{G}$, whereas at $k \geq k_{\text{lim}}$ a second one appears due to the three zero crossings of φ.

However, if the load is reduced during operation the equivalent load resistance increases and a pole-splitting will be inevitable. To remain functional at a high magnetic coupling or under low load conditions, an IPT controller must be designed accordingly, i.e. it must also operate if a pole-splitting occurs.

IV. Control Algorithms

A full-bridge inverter is typically used for the supply of a resonant tank in the kW-range. Possible control methods include a variation of either the phase shift between the two converter bridge legs, the switching frequency or the dc-link voltage. Since a variable dc-link voltage would require an additional buck stage to feed the dc-link it is not treated further in this work. The more common control methods, phase shift control and frequency control, are discussed below. Additionally, a dual control method is proposed for use in an IPT system.

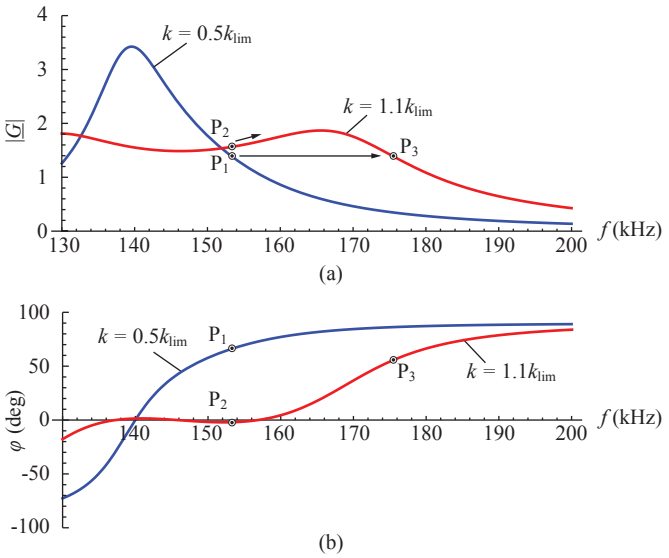

Fig. 4. Effect of a sudden change of the magnetic coupling or the load on the magnitude of the voltage transfer function (a) and on the phase of the input impedance (b). Starting from operating point P_1, a frequency controller would operate in P_2 after a step change of the coupling or the load, i.e. in a capacitive operating point. A dual controller would move to P_3 while keeping the circuit inductive.

A. Phase Shift Control

A possible control scheme for a full-bridge inverter is the operation at a constant switching frequency f_s with a variable phase shift of the two bridge legs. This allows producing an inverter output voltage with a variable pulse width and, thus, a variable amplitude of the fundamental.

Theoretically, this would offer the possibility to control the output power of the resonant converter. However, applying this control method aggravates ensuring soft-switching of the semiconductor devices, because inductive operation is not guaranteed in the vicinity of the resonant frequency if a pole-splitting occurs. Therefore, high switching losses resulting from reverse recovery of the anti-parallel diodes $D_{1..4}$ occur. Additionally, the reduction of the voltage amplitude requires a higher primary current to deliver the same amount of power to the load. This results in an increase of the conduction losses in the switches and the resonant circuit and the system efficiency would be reduced. For these reasons, this control scheme is not further investigated.

B. Frequency Control

A typical control method for IPT systems is to adapt the switching frequency at a constant phase shift of 180° of the bridge legs. To control the output power, the switching frequency is increased to operate in the region where the magnitude $|\underline{Z}_{\text{in}}|$ is higher and the primary current i_1 as well as the transmitted power are reduced. From Fig. 3(b)-(c), it can be concluded that this requires operation at frequencies higher than all three zero crossing frequencies of φ, which may be up to 20-30% higher than ω_0.

If sudden changes of the magnetic coupling or the load occur, this becomes difficult to guarantee: because of the change in either k or k_{lim} (cf. (8)), the condition $k < k_{\text{lim}}$ may be violated. This is shown in Fig. 4. Assuming the system has settled to operating point P_1, a frequency controller would initially keep the switching frequency constant even if a sudden change of the magnetic coupling or the load occurs. It would therefore be moved to P_2, where it would start

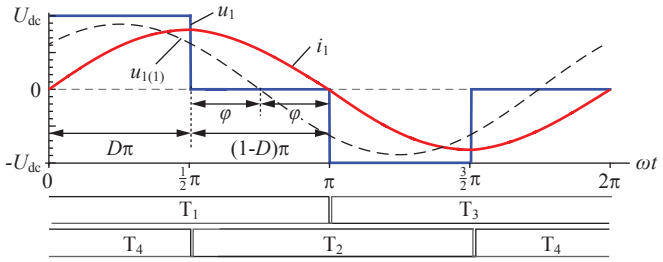

Fig. 5. Simulated waveforms of the inverter output voltage u_1 and the primary current i_1, and calculated fundamental component of the inverter output voltage $u_{1(1)}$ for the dual control method. The only hard switching is the turn-off of the devices T_4 and T_2 at $D\pi$ and $(D+1)\pi$, respectively. The MOSFET internal diodes $D_{1..4}$ only conduct during the commutation intervals (not shown), afterwards the corresponding MOSFETs are turned on and carry the current.

increasing the frequency as indicated in Fig. 4(a) to compensate for the increased output voltage, causing the output voltage to rise even further. During the time it takes to settle in P_3, the circuit can become capacitive and hard switching of the converter can occur.

C. Dual Control

For series and series-parallel resonant converters a combination of the phase shift and the frequency control methods termed dual control is known in literature [19]–[21]. In this control scheme, the zero crossings of the primary current are detected and used to trigger the gate signals for the switches of the leading bridge leg (T_1, T_3). After the active interval determined by the duty cycle D, the switch of the lagging bridge leg (T_2, T_4) is turned off and the current is commutated to the anti-parallel diode of the opposite switch, which can therefore be turned on while the diode is conducting. As a result, the leading bridge leg is operated with Zero Current Switching (ZCS) and Zero Voltage Switching (ZVS) at turn-on and turn-off. The lagging bridge leg is operated with ZVS at all switching instants. Simulated waveforms resulting from this control scheme are shown in Fig. 5.

Apart from the soft-switching performance, another key advantage of this method compared to the classical frequency control is the inherently ensured inductive operation due to the coupling of the duty cycle to the phase of the input impedance [21]

$$(1-D)\pi \equiv 2\varphi. \tag{9}$$

The resonant tank will automatically oscillate at a frequency where this relation is fulfilled. Referring to Fig. 4, at a rapid change of the coupling or the load a dual controller would move from operating point P_1 to operating point P_3 without passing through P_2, thus inductive operation of the inverter is maintained.

V. Performance Comparison

In order to evaluate the performance of the presented control methods, analytical models were used to determine the voltages and currents in the resonant tank and to calculate the losses in the different components of the system. A cut through the landscape of results is shown in Fig. 6 and discussed along with a comparison of the most important performance-influencing parameters (cf. Fig. 7) in the remainder of this paper.

A. Coil and Capacitor Stress

The overall system efficiency η is mainly influenced by the component stresses in the resonant tank, namely the peak inductor currents $\hat{I}_1$, $\hat{I}_{L_2}$, the peak primary capacitor voltage $\hat{U}_{C_1}$ and the peak parallel capacitor current $\hat{I}_{C_2}$. The peak current in the primary capacitor is equal to $\hat{I}_1$ and the peak value of the voltage over the parallel capacitor C_2 is given by the output voltage U_{out}.

As shown in Fig. 7, the dual control method leads to a reduction of the coil and capacitor currents. With the frequency control method, a reduction of the output voltage can only be achieved with an increase of the switching frequency, due to the shape of the magnitude of the voltage transfer function (cf. Fig. 3). With the dual control method, the reduced pulse width of the inverter output voltage leads to a reduction of the fundamental

$$\underline{\hat{U}}_{1(1)} = \frac{4}{\pi} U_{\text{dc}} \sin\left(\frac{D\pi}{2}\right). \tag{10}$$

Therefore, at reduced output voltages dual control allows operating at lower switching frequencies, where $|\underline{G}|$ is higher. This is evident by comparing Fig. 6(a) and 6(d). As a result, a less inductive operating point is obtained for the same output power, which results in a reduced primary current. Due to the lowered induced voltage on the secondary, this also leads to a reduction of the secondary coil current and the current in the secondary capacitor. The primary capacitor voltage

$$\underline{\hat{U}}_{C_1} = \frac{\hat{I}_1}{\mathrm{j}\omega_s C_1} \tag{11}$$

remains almost constant during this process due to the reduction of both, frequency and primary current.

B. Semiconductor Stress

The conduction losses in the devices of the full-bridge inverter can be calculated from the RMS value of the conducted current. For MOSFETs, these can be calculated analytically with the assumption of a sinusoidal primary current and the $R_{\text{DS(on)}}$ of the device. For a first analysis, the amplitude of the switched current $\hat{I}_{1,\text{off}}$ is a good indicator for the switching losses. Due to the reduced primary current, also the RMS current in the devices and $\hat{I}_{1,\text{off}}$ are lower for the dual control method. This indicates lower conduction losses and reduced switching losses, also for the devices of the lagging bridge leg that are conducting a current at turn-off. For the power level considered in this work, MOSFETs are the most suitable switching devices and switching losses can be neglected in a fist step. However, if a lower switching frequency and IGBTs are used also the dynamic effects influencing the switching losses at ZCS must be considered for an optimization of the system [22], [23].

The calculation of the losses in the diode rectifier requires a more detailed model than the fundamental frequency analysis presented in Section III. However, as they are expected to exhibit only negligible differences for the two control schemes they are not included in this evaluation.

C. Efficiency

An approximative calculation of the total losses in the system was used to estimate the system efficiency η in the operating area. The result is shown in Fig. 6(f). For this calculation, an assumed coil quality factor of $Q = 300$ was used to calculate the resistance of the coils and an estimated Equivalent Series Resistance (ESR) was used to calculate the capacitor losses. For the semiconductors, only

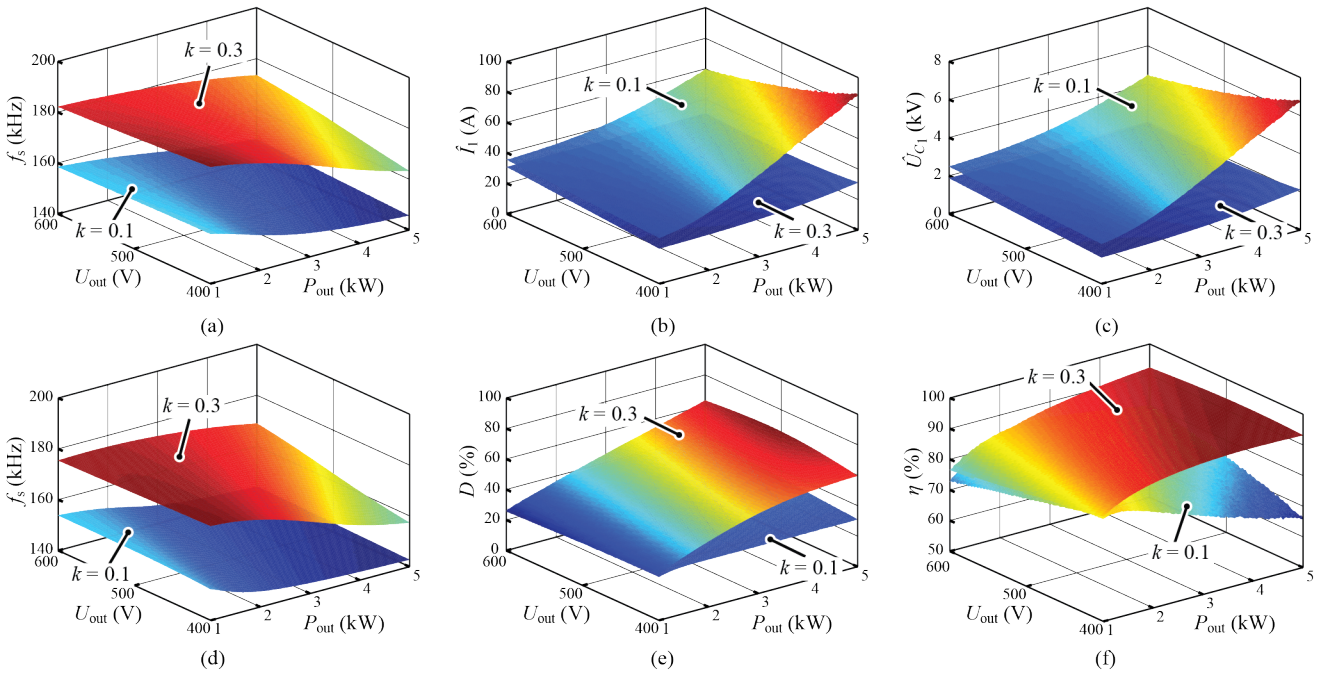

Fig. 6. Switching frequency f_s, primary peak current $\hat{I}_1$ and primary capacitor voltage $\hat{U}_{C_1}$ for the frequency control method (a)-(c); switching frequency f_s, duty cycle D, and approximated system efficiency η for the dual control method (d)-(f).

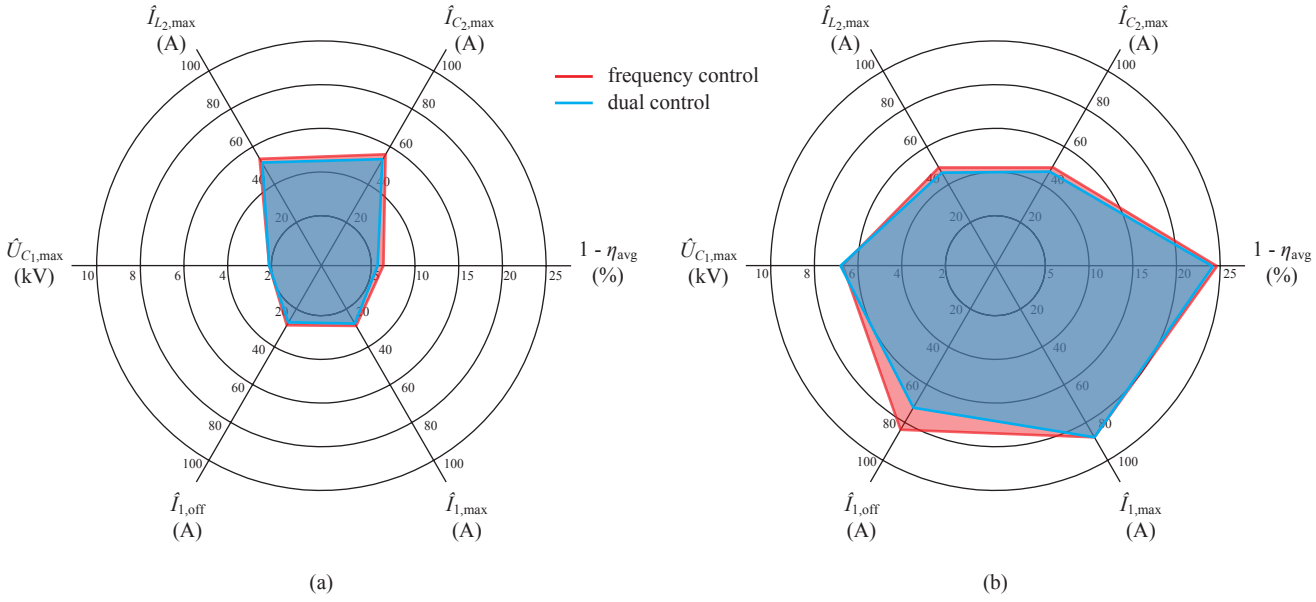

Fig. 7. Comparative evaluation of the control methods for $k = 0.3$ (a) and $k = 0.1$ (b). The maximum values of the currents $\hat{I}_{1,max}$, $\hat{I}_{1,off}$, $\hat{I}_{L_2,max}$, $\hat{I}_{C_2,max}$ and the voltage $\hat{U}_{C_1,max}$ are shown. The total losses were derived with an approximative calculation and averaged over the operating range.

conduction losses of a 600 V-rated MOSFET with $R_{DS(on)} = 165\,m\Omega$ at 125 °C were included.

Clearly, the efficiency is not constant over the operating area (cf. Fig. 6(f)). For a future optimization of the system, a cost function could be derived from the calculated efficiency values and a load profile could be used as a weighting function. The load profile could for instance include statistical information about the charging requirements of the battery. As an example, the average relative losses $1-\eta_{avg}$ indicated in Fig. 7 were calculated for operation at maximum output power and a uniform distribution of the output voltage. The result shows that the dual control method and the frequency control method lead to a similar performance.

D. Controllability

As previously mentioned in Section IV-C, the dual control method guarantees inductive operation, whereas with a frequency controller capacitive switching could occur after rapid changes of the load or the magnetic coupling. This is an advantage of the dual control method.

At a short circuit of the load, the influence of the resonance capacitor C_2 on the secondary vanishes and the input impedance of the primary gets inductive. Therefore, the primary current rises slowly and the short circuit can be handled safely. This applies advantageously for both control methods.

Due to the highly selective shape of the voltage transfer function, the control outputs for both control methods require a high precision, especially at low values of the magnetic coupling. It must be ensured that the small variations of the switching frequency and the duty cycle can be realized in practice.

VI. Conclusion & Future Work

In this paper, the frequency characteristics of the series-parallel resonant converter used in an IPT application are discussed. Two control methods, frequency control and dual control are analyzed and compared based on numerical calculations. It is shown that the performance of the dual control method leads to a very similar performance compared to frequency control method which typically used for IPT systems. As the dual control method offers a number of advantages in terms of the controllability of the system, it is therefore the preferable solution.

Future work will include an experimental verification of these theoretical results. Additionally, a holistic optimization of the IPT system is still missing in the literature. With the models derived for the calculations presented in this paper, the basis for the evaluation of an IPT system design is given and an optimization routine could be used to find an optimal design in respect of a given load profile.

Acknowledgment

The authors would like to thank ABB Switzerland Ltd. for their funding and for their support regarding many aspects of this research project.

References

[1] J. C. Schuder, J. H. Gold, and H. E. Stephenson, "An inductively coupled rf system for the transmission of 1 kW of power through the skin," *IEEE Transactions on Bio-Medical Engineering*, vol. 18, no. 4, pp. 265–273, 1971.

[2] J. C. Schuder, "Powering an artificial and heart: birth and of the inductively and coupled-radio frequency system in 1960," *Artificial Organs*, vol. 26, no. 11, pp. 909–915, 2002.

[3] G. Vandevoorde and R. Puers, "Wireless energy tranfer for stand-alone systems: A comparison between low and high power applicability," *Sensors A*, vol. 92, no. 1-3, pp. 305–311, 2000.

[4] K. Van Schuylenbergh and R. Puers, *Inductive Powering: Basic Theory and Application to Biomedical Systems*, 1st ed. Springer Science, 2009.

[5] B. Lenaerts and R. Puers, *Omnidirectional Inductive Powering for Biomedical Implants*, 1st ed. Springer Science, 2009.

[6] K. Finkenzeller, *RFID-Handbook: Fundamentals and Applications in Contactless Smart Cards, Radio Frequency Identification and Near-Field Communication*, 3rd ed. John Wiley & Sons, 2010.

[7] E. Waffenschmidt and T. Staring, "Limitation of inductive power transfer for consumer applications," in *Proc. of the 13th European Conference on Power Electronics and Applications (EPE)*, 2009, pp. 1–10.

[8] G. A. Covic, G. Elliott, O. H. Stielau, R. M. Green, and J. T. Boys, "The design of a contact-less energy transfer system for a people mover system," in *Proc. of the International Conference on Power System Technology (PowerCon)*, vol. 1, 2000, pp. 79–84.

[9] J. Huh, S. W. Lee, W. Y. Lee, G. H. Cho, and C. T. Rim, "Narrow-width inductive power transfer system for online electrical vehicles," *IEEE Transactions on Power Electronics*, vol. 26, no. 12, pp. 3666–3679, 2011.

[10] A. L. Jesús Sallán, Juan L. Villa and J. F. Sanz, "Optimal design of ICPT systems applied to electric vehicle battery charge," *IEEE Transations on Industrial Electronics*, vol. 56, no. 6, pp. 2140–2149, 2009.

[11] M. Broussely, *Industrial Applications of Batteries: From Cars to Aerospace and Energy Storage*. Elsevier, Amsterdam, 2007.

[12] C.-S. Wang, O. H. Stielau, and G. A. Covic, "Design considerations for a contactless electric vehicle battery charger," *IEEE Transactions on Industrial Electronics*, vol. 52, no. 5, pp. 1308–1314, 2005.

[13] C.-S. Wang, G. A. Covic, and O. H. Stielau, "Power transfer capability and bifurcation phenomena of loosely coupled inductive power transfer systems," *IEEE Transactions on Industrial Electronics*, vol. 51, no. 1, pp. 148–157, 2004.

[14] ——, "Investigating an LCL load resonant inverter for inductive power transfer applications," *IEEE Transactions on Power Electronics*, vol. 19, no. 4, pp. 995–1002, 2004.

[15] R. Bosshard, J. Mühlethaler, J. W. Kolar, and I. Stevanović, "The η-α-pareto front of inductive power transfer coils," in *Proc. of the 38th IEEE Industrial Electronics Conference (IECON)*, 2012.

[16] R. L. Steigerwald, "A comparison of half-bridge resonant converter topologies," *IEEE Transactions on Power Electronics*, vol. 3, no. 2, pp. 174–182, April 1988.

[17] A. K. Gregory Ivensky and S. Ben-Yaakov, "An RC load model of parallel and series-parallel resonant DC-DC converters with capacitive output filter," *IEEE Transactions on Power Electronics*, vol. 14, no. 3, pp. 515–521, 1999.

[18] P. E. K. Donaldson, "Frequency-hopping in r.f. energy-transfer links," *Electronics & Wireless World*, pp. 24–26, Aug. 1986.

[19] J. A. Sabate, M. M. Jovanovic, F. C. Lee, and R. T. Gean, "Analysis and design-optimization of LCC resonant inverter for high-frequency AC distributed power system," *IEEE Transations on Industrial Electronics*, vol. 42, no. 1, pp. 63–71, 1995.

[20] H. Pinheiro, P. K. Jain, and G. Joos, "Self-sustained oscillating resonant converters operating above the resonant frequency," *IEEE Transactions on Power Electronics*, vol. 14, no. 5, pp. 803–815, 1999.

[21] F. da Silveira Cavalcante, "High output voltage series-parallel resonant dc-dc converter for medical x-ray imaging applications," Ph.D. dissertation, Swiss Federal Institute of Technology Zurich (ETHZ), 2006.

[22] P. Ranstad and H.-P. Nee, "On dynamic effects influencing IGBT losses in soft-switching converters," *IEEE Transactions on Power Electronics*, vol. 26, no. 1, pp. 260–271, January 2011.

[23] G. Ortiz, D. Bortis, J. W. Kolar, and O. Apeldoorn, "Soft-switching techniques for medium-voltage isolated bidirectional DC/DC converters in solid state transformers," in *Proc. of the 38th IEEE Industrial Electronics Conference (IECON)*, 2012.